

Photon total angular momentum manipulation

Lang Li,^{a,b,c} Yingchi Guo,^{a,b,c} Zhichao Zhang,^{a,b,c} Zijun Shang,^{a,b,c} Chen Li,^{a,b,c} Jiaqi Wang,^{a,b,c} Liliang Gao,^{a,b,c} Lan Hai,^{a,b,c} Chunqing Gao,^{a,b,c} and Shiyao Fu^{a,b,c,*}

^aBeijing Institute of Technology, School of Optics and Photonics, Beijing, China

^bMinistry of Education of the People's Republic of China, Key Laboratory of Photoelectronic Imaging Technology and System, Beijing, China

^cMinistry of Industry and Information Technology of the People's Republic of China, Key Laboratory of Information Photonics Technology, Beijing, China

Abstract. As an inherent degree of freedom, total angular momentum (TAM) of photons consisting of spin angular momentum and orbital angular momentum has inspired many advanced applications and attracted much attention in recent years. Probing TAM and tailoring beam's TAM spectrum on demand are of great significance for TAM-based scenarios. We propose both theoretically and experimentally a TAM processor enabling tunable TAM manipulation. Such a processor consists of a set of quasi-symmetric units, and each unit is composed of a couple of diffraction optical elements fabricated through polymerized liquid crystals. Forty-two single TAM states are experimentally employed to prove the concept. The favorable results illustrate good TAM state selection performance, which makes it particularly attractive for high-speed large-capacity data transmission, optical computing, and high-security photon encryption systems.

Keywords: vortex beams; orbital angular momentum; spin angular momentum; total angular momentum tailoring.

Received Apr. 29, 2023; revised manuscript received Jun. 7, 2023; accepted for publication Aug. 3, 2023; published online Aug. 30, 2023.

© The Authors. Published by SPIE and CLP under a Creative Commons Attribution 4.0 International License. Distribution or reproduction of this work in whole or in part requires full attribution of the original publication, including its DOI.

[DOI: [10.1117/1.AP.5.5.056002](https://doi.org/10.1117/1.AP.5.5.056002)]

1 Introduction

The pioneering works of Beth and Mechanical¹ and Allen et al.² illustrated that photons can possess two distinct forms of angular momentums (AMs), spin angular momentum (SAM), and orbital angular momentum (OAM). SAM has two eigenvalues $\sigma = \pm 1$, corresponding to the right and left circular polarizations of a macroscopic beam,¹ while the eigenvalue l of OAM, also known as topological charge, can be any integer. The eigenvalue l determines the helical wavefront as $\exp(il\varphi)$, where φ is the azimuthal angle.^{2,3} Originally, researchers focused more on OAM beams, namely, optical vortices, due to their enormous potential in large-capacity data transmission,⁴⁻⁷ optical tweezers,⁸ rotation detection,⁹ and other applications.¹⁰⁻¹² Recently, photon total angular momentum (TAM),¹³ the sum of SAM and OAM under paraxial approximation, came into view. The most well-known TAM carried beam is a vectorial vortex beam featuring anisotropic polarization distribution and a complex wavefront.^{14,15} Currently, TAM has inspired many advanced applications, ranging from classical to quantum physics such as laser processing¹⁶ and motion detection.¹⁷ Moreover, TAM

provides 2 degrees of freedom (DoFs), SAM and OAM; thus it is of great significance in achieving higher-dimensional entanglements.^{18,19}

Processing TAM components on demand is a crucial basis for TAM applications. In other words, for a TAM beam, one can extract corresponding TAM photons and drop out irrelevant TAM photons selectively, which can be regarded as a TAM filter, analogous to a common wavelength/frequency filter. Such manipulation is of great significance, especially as the receiver for TAM-based communications, remote detection, and optical computing. TAM filtration can be accomplished through simultaneous SAM and OAM filtration. SAM filtration is simple and can be implemented through polarization elements such as wave plates, whereas OAM filtration is intricate. In the past two decades, much effort has been devoted to excavating more effective schemes for OAM probing and extraction, for instance, by probing and recognizing OAM modes through diffraction optical elements (DOEs),²⁰⁻²⁵ interferometers,²⁶ neural networks,^{27,28} and so on. Various OAM sorters have also been developed such as the Mach-Zehnder interferometer²⁹⁻³¹ and log-polar transformation-based elements,³²⁻³⁶ enabling the tunable OAM filter.³⁷ Recently, metamaterials with polarization modulation characteristics have been introduced for photon SAM and OAM

*Address all correspondence to Shiyao Fu, fushiyao@bit.edu.cn

processing, accomplishing TAM separation.^{38–40} Nevertheless, extracting or filtering desired TAM states from a beam is still a challenge.

In this work, we demonstrate a TAM manipulator for photons that enables selective TAM extraction. The TAM filter has a quasi-symmetric structure, where the incident beam can be seen as propagating through TAM separation unit twice, in opposite directions. In the TAM separation section, a couple of DOEs are fabricated through polymerized liquid crystals (LCs), designed from wavefront-copy embedded log-polar coordinate mapping, leading to little cross talk of OAM separation. Meanwhile, these DOEs introduce conjugated phase modulations for opposite SAM components and thus separate each TAM state spatially. A spatial filter is employed to reserve or block single or multiple TAM states, and then the separated beams are recovered through the reverse TAM separation unit. Such a process maps the incident beam from spatial domain to “position-TAM domain” for easy filtering, and then converts it back into the spatial domain again. To prove the principle, 42 single TAM states are involved to evaluate the mode purity reduction for a nonfiltering test; 16 modes are used for selective blocking tests. The simulation and experiment are accomplished with a favorable performance.

2 Concept of the TAM Manipulation

As mentioned above, a single TAM mode, also known as a separable state, is written in direct product form as $|\sigma\rangle|l\rangle$. A TAM beam $|\psi\rangle$ could simultaneously contain multiple TAM states, which has the form of $|\psi\rangle = \sum_{\xi} \sum_{\kappa} \alpha_{\xi}^{\kappa} |\sigma_{\xi}\rangle |l_{\kappa}\rangle$ with α_{ξ}^{κ} the complex coefficient, namely, multiplexed TAM states. Here the SAM component $|\sigma_{\xi}\rangle$ has two eigenvalues, $\sigma = +1$ and $\sigma = -1$, corresponding to the right and left circular polarizations, and can be denoted as $|R\rangle$ and $|L\rangle$, respectively. The OAM component $|l_{\kappa}\rangle \propto \exp(il_{\kappa}\varphi)$ with φ the azimuthal angle and κ can be any integer. The TAM represents the AMs of each photon as $J = (\sigma + l)\hbar$ under paraxial approximation with \hbar the reduced Planck constant.

The proposed TAM manipulator is expected to retain or eliminate specific TAM components as needed. Figure 1 sketches the concept and principle of the TAM manipulator. For instance, an incident beam comprises four TAM states, while what we want is two of them. After passing through a

spatial filter, only the desired TAM components are reserved, while others are removed. For this purpose, each TAM state must be exactly extracted, where a feasible way is to separate various TAM states with high accuracy. Specifically speaking, each single TAM state $|\sigma\rangle|l\rangle$ of the incident beam could be diffracted to different positions in the observation plane, in which each single TAM mode can be blocked or passed, enabling selective TAM manipulation. That is, some of the TAM states are filtered. The separated modes are then combined through a symmetric unit and reconverted to a TAM beam again to accomplish the TAM manipulator.

2.1 Manipulating TAM States on Demand: TAM Separation

TAM state separation could be viewed as simultaneous separation of SAM and OAM. The SAM separation can be accomplished through a polarization grating, the essence of which is a geometric phase modulation result from the photon spin Hall effect.⁴¹ As for OAM separation, its schemes are diversified,^{29–35} such as optical transformations^{32,33} and D²NN.^{28,42} Obviously, integrating polarization grating and log-polar transformation elements enable SAM and OAM separation simultaneously; thus, TAM separation is available. Actually, in the past decade, based on this idea, various TAM separation schemes have been proposed.^{38–40} However, they may face trouble if employed in a TAM filter, for instance, adjacent mode overlap, low dynamic range, and small diameter. It is certain that the greater the effectiveness of the TAM separation is, the more straightforward the mode selection becomes.

High-performance SAM separation can be achieved easily through geometric phase optical elements (GPOEs). The conversion efficiency of a GPOE can reach 100% under half-wave conditions, and their thickness is in the wavelength magnitude. A GPOE with spatially varying main-axis orientations according to ϕ can transform the incident circular polarization to its opposite; namely, the SAM state is reversed. Meanwhile, an additional phase is introduced as $\pm 2\phi$ for incident LCP and RCP, respectively. Obviously, embedding a linear gradient phase denoted by $2\phi = k \sin(\theta x)$, where k and θ are the wavenumber and the period of linear gradient phase, respectively, the two

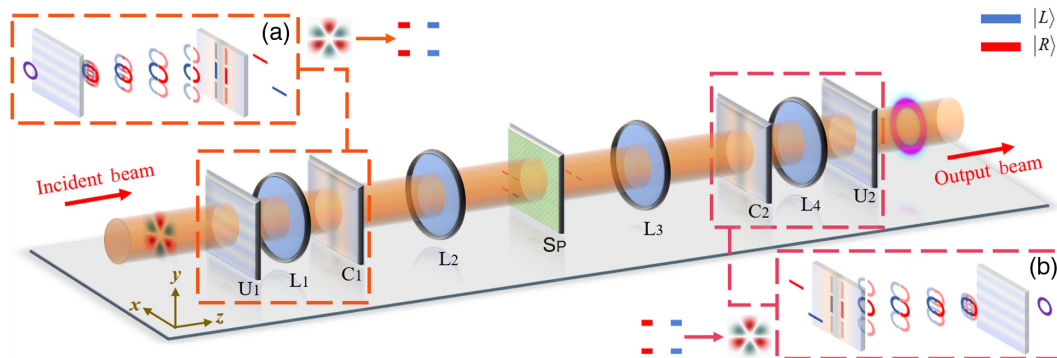


Fig. 1 Concept of a TAM manipulator: structure of a TAM carried beam passes through the TAM manipulator for filtering. Beam propagation diagram of (a) the TAM separator and (b) the TAM reverser. U₁ and U₂, unwrappers; C₁ and C₂, correctors; L₁ to L₄, lenses; Sp, separation (filtered) plane.

SAM components will be diffracted to different spatial positions and thus be effectively separated.

For separating OAM DoF, the fan-out scheme, proposed by Mirhosseini et al.,³³ is employed. Such a fan-out scheme is actually the wavefront-copy associated with log-polar coordinate transformation. It reduces the spatial spectral range of the converted beam, thus achieving a narrower pattern width after separation. Previous research has proved that OAM separation is still feasible when the unwrapper or corrector adopts an opposite modulation phase, while the separated states from positive and negative modulation are centrosymmetric on the separating plane.⁴³ Therefore, separating OAM mode with little cross talk through the geometric phase modulation is available (see Note 1 in the [Supplementary Material](#) for details).

Based on the above fan-out OAM separation and geometric phase modulation, we propose a precise TAM separation scheme. The TAM separator is implemented by a couple of GPOEs working as an unwrapper and a phase corrector. As shown in Fig. 1, the mode separation and phase correction GPOEs, referred to as the unwrapper and the corrector for simplicity, associated with two lenses, form the TAM separator. The unwrapper (U_1), the first lens (L_1), the corrector (C_1), and the second lens (L_2) are placed in sequence along the z axis. The unwrapper and the corrector are, respectively, located in the front and rear focal planes of the lens L_1 , whose corresponding coordinates are denoted as (x, y) and (u, v) , separately. And the lens L_2 is used to focus the light field passing through the corrector. Fusing the modulation phases corresponding to SAM and OAM separation, the additional geometric phase of the unwrapper element is described by

$$\begin{aligned} \phi_1(x, y) = & \frac{2\pi a}{\lambda f_1} \left[y \arctan\left(\frac{y}{x}\right) - x \ln\left(\frac{\sqrt{x^2 + y^2}}{b}\right) + x \right] \\ & + \arctan\left[\frac{\sum_{q=-N}^N c_q \sin\left(\frac{2\pi\theta}{\lambda} qy + \zeta_q\right)}{\sum_{q=-N}^N c_q \cos\left(\frac{2\pi\theta}{\lambda} qy + \zeta_q\right)} \right] + \frac{\delta_1 x}{\lambda f_1}. \end{aligned} \quad (1)$$

The first term of Eq. (1) represents the log-polar coordinate transformation,³² where λ is the wavelength of the incident beam, f_1 is the focal length of lens L_1 , and a and b are the transformation scaling parameters. Then the arc tangent term refers to the wave copying with the maximum diffraction order N of the copy process and θ is the separation angle. c_q and ζ_q are the complex coefficients for adjusting different diffraction orders.³³ The last term is the linearly gradient phase for SAM separation, where δ_1 determines the separation distance along the horizontal.

Take an incident TAM beam $|\psi\rangle = \sum_{\xi=-1,1} \sum_{\kappa=-4,+4} \alpha_{\xi}^{\kappa} |\sigma_{\xi}\rangle |I_{\kappa}\rangle$ as an example; after passing through the unwrapper and focused by lens L_1 , it is unwrapped and two observed SAM components are centrosymmetric around the origin (see Note 1 in the [Supplementary Material](#) for details). However, an inevitable phase distortion is introduced by the unwrapper and also the propagation from the front to back focal planes of lens L_1 . Therefore, a correction phase calculated by the stationary phase approximation⁴⁴ is necessary,

$$\begin{aligned} \phi_2(u, v) = & \sum_{q=-N}^N \text{rect}\left(\frac{v - qd}{d}\right) \left[-\frac{bd}{\lambda f_1} \exp\left(\frac{-2\pi|u| + \delta_1}{d}\right) \right. \\ & \left. \times \cos\left(\frac{2\pi v}{d}\right) + \varphi_q(q) \right] + \frac{\delta_2 u}{f_2}. \end{aligned} \quad (2)$$

In Eq. (2), $d = 2\pi a$ denotes the transformed fringe length from OAM modes. $\varphi_q(q)$ is used to compensate for the additional phase introduced in the wave-copying process. The last term is essential to guarantee SAM separation with zero cross talk, enabling the processor to support as many TAM states as possible. f_2 is the focal length of lens L_2 ; δ_2 works similar to δ_1 . The $\text{rect}()$ function is described as follows:

$$\text{rect}(x) = \begin{cases} 1, & |x| < 1/2 \\ 0, & |x| \geq 1/2 \end{cases}. \quad (3)$$

When passing through the TAM separator, the incident TAM beam $|\psi\rangle$ is converted into plane waves with different linearly gradient phases. Finally, they are focused by lens L_2 , and photons from various single TAM components are located in different positions. The horizontal separation distance between two SAM components becomes further apart. Both of them contain their corresponding OAM modes, distributed at vertical intervals (see Note 1 in the [Supplementary Material](#) for details). So far, the TAM states are completely separated, providing a path for subsequent TAM operation.

To achieve the above functions, we fabricate the unwrapper and the corrector through polymerized LCs, as displayed in Fig. 2. The main-axis orientation distributions of the unwrapper and corrector are given by $\alpha_1(x, y) = \phi_1(x, y)/2$ and $\alpha_2(u, v) = -\phi_2(u, v)/2$, as shown in Figs. 2(a) and 2(b). Figures 2(c)–2(f) present the inspection of the fabricated GPOEs under a polarized optical microscope.

2.2 Manipulating TAM States on Demand: TAM Reverser

After blocking the redundant TAM states at the rear focal plane of lens L_2 , the selected states need to be reconverted into the initial incident form. One of the most straightforward approaches is making the beam pass through a structure symmetrical with the TAM separator proposed above, for instance, using an element to reflect the separated beam back to the TAM separator. Although this method has advantages such as a compact structure and element saving, it does not apply to the TAM situation due to the spatial separation of SAM modes.

For the reflection schemes, lens L_2 and the reflector constitute an equivalent 4- f system, whose input and output planes correspond to the (u, v) planes of corrector and reversal corrector, respectively. It is obvious that the output beam is centrosymmetric with the input, and the linear gradient phases of it in u axis will be reversed when passing through the equivalent 4- f system. As the main-axis orientation angle distribution of the corrector is asymmetrical in the u axis, the reversed-corrector must be rotated 180 deg to achieve reversal phase modulation. While the SAM modes will overlap at the front focal plane of the reversal first lens, the reversed-unwrapper does not require rotation. Therefore, the TAM reverser cannot reuse the TAM separator (see Note 2 in the [Supplementary Material](#) for details),

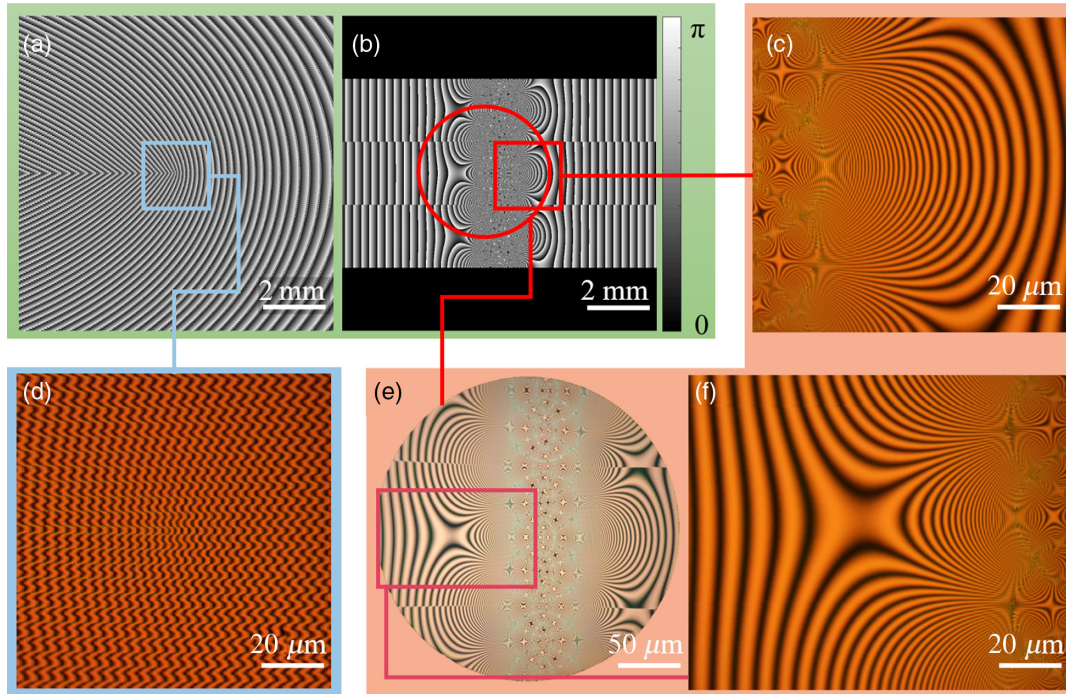


Fig. 2 Details of the fabricated GPOEs. Main-axis orientation angle distributions of the designed elements for (a) the unwrapper and (b) the phase corrector. (e) Inspection of the corrector-center via polarized optical microscope. Inspection detail of the (d) unwrapper central zone and (f), (c) the corrector left and right regions.

and a transmissive scheme must be employed here to recover TAM beams.

The right part of Fig. 1 gives the structure of the TAM reverser, and the order of these elements along the z axis is the third lens (L_3), rotated-corrector (C_2), the fourth lens (L_4), and unwrapper (U_2). The TAM separation plane (Sp) and the rotated-corrector are located at the front and rear focal planes of lens L_3 , respectively. Meanwhile, the rotated-corrector and unwrapper are located at the front and back focal planes of lens L_4 , separately.

3 Results

As shown in Fig. 1, the photon TAM manipulator consists of a TAM separator and a reverser. The distributions of input TAM beams after each GPOE are given in Note 3 in the [Supplementary Material](#). In our design, the range of TAM separation is SAM modes $\sigma = -1, 1$, OAM modes $l_k = -10, -9, \dots, +10$, totaling 42 single separable TAM states. The simulated and experimental incident beam is a horizontally polarized Gaussian beam carrying a spiral phase, while the Laguerre-Gauss (LG) beam is a theoretical situation. Obviously, the efficiency of the TAM separator is the basis of the photon TAM processor, and a concept of optical finesse is adopted for quantitative evaluation.²¹ In simulation cases, the optical finesse is calculated as 2.63 and 2.60 for $\sigma = 1$ and $\sigma = -1$, while it drops down to 1.03 and 1.79 for $\sigma = 1$ and $\sigma = -1$ in experiment. The deviation can be ascribed to the fabricating error of GPOEs and the slight misalignment between these GPOEs in experiment. More detail on the separation evaluation is presented in Note 4 in the [Supplementary Material](#).

Though the experimental TAM separation efficiency is still nonideal, it is sufficient for further TAM processor experiments. To evaluate the performance of the processor, a series of numerical simulations and experiments are carried out. The complete optical details are given in Note 5 in the [Supplementary Material](#).

Considering the quasi-symmetric structure of the concept, it is imperative to verify the consistency of the optical characterization of the input and output beams when there is no occlusion on the TAM separation plane. Figure 3(a) shows the results of single-mode TAM beams $|\psi_1\rangle = |L\rangle - 7\rangle$ and $|\psi_2\rangle = |R\rangle + 8\rangle$ passing through the manipulator (other results are given in Note 6 in the [Supplementary Material](#)). The numerical simulation indicates that the intensities of separation (filter) plane are in accordance with the former theory. However, though the phase distributions of the output beams meet the expectation, the intensities are imperfect. Therefore, evaluating the TAM mode purity loss passing through the processor without filtering is necessary. Figure 3(b) shows the output TAM spectrum for the inputs of those single TAM states. The simulation result is acceptable that the average loss of mode purity is 2.63%, whereas the experimental result increases it to 10.12%. With the application of high-efficiency GPOEs, the insertion loss of the system is estimated to be 0.83 dB when there is no filtering. In a word, for the straight-through cases, the outputs from the proposed TAM processor are nearly identical with inputs in simulation, while the experiment result is slightly deviated.

Further experiments of multi-TAM states incident are carried out. These input TAM states are $|\Psi_l\rangle = (|L\rangle + |R\rangle)(|l\rangle + |-l\rangle)$, $l = 5, 8, 9, 10$, namely, a horizontally linearly polarized twofold multiplexed OAM beam. The cases of both

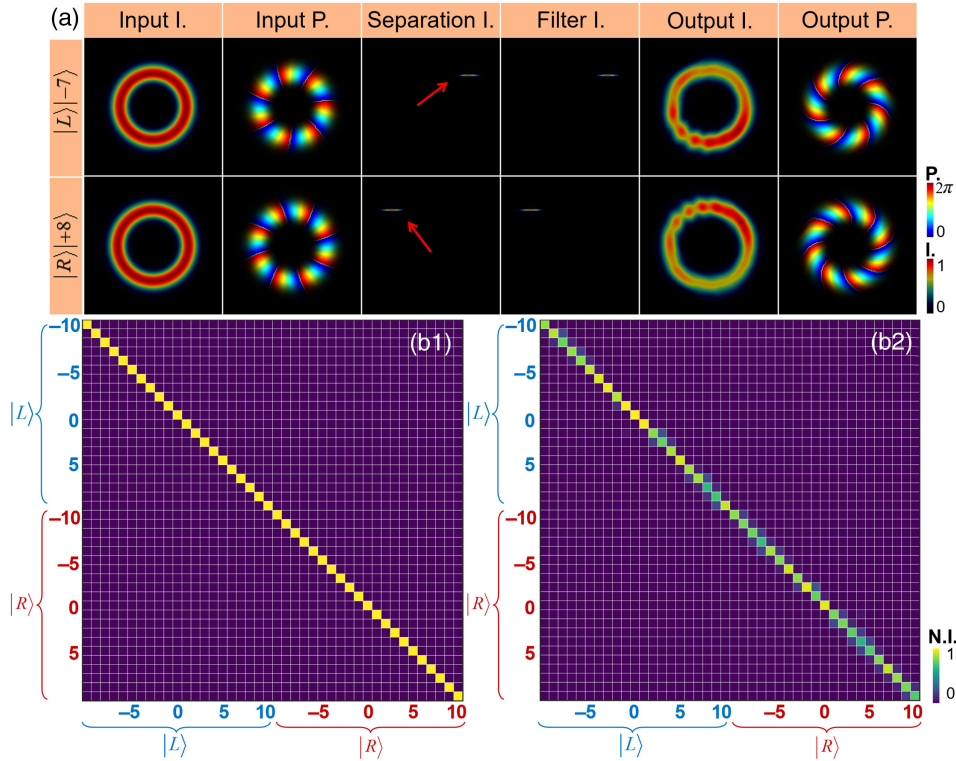


Fig. 3 Performance of the TAM manipulator in straight-through cases. (a) The numerical simulation of various observing planes for incident beams $|\psi_1\rangle = |L\rangle_{-7}$ and $|\psi_2\rangle = |R\rangle_{+8}$. (b1) The simulated TAM spectra confusion matrix of the output beams versus input beams, where left and right circular polarizations are described as blue and red font color in axes, separately, and the OAM modes are represented by numbers. (b2) The corresponding experimentally measured results.

straight-through and selective-blocking are given for better comparison. Figure 4(a) shows the intensities' distributions of the input, separation (filter), and the output plane for the two cases. Obviously, the intensities of outputs are consistent with the inputs at the straight-through cases, and the distributions of the separated plane conform to the previous theoretical analysis. To quantifiably evaluate the consistency of the TAM spectrum after and before passing through the processor, TAM spectrum fidelity F , analogous to quantum conception, is introduced and denoted by

$$F_{a,b} = \langle \psi_b | (|\psi_a\rangle \langle \psi_a|) | \psi_b \rangle. \quad (4)$$

In Eq. (4), $|\psi_i\rangle = (p_L \ p_R)^T$ is the TAM state vector, where p_L and p_R are the relative OAM intensity spectrum vector for the left and right circular polarizations, respectively. i has three symbols: “theo,” “sim,” and “exp,” corresponding to theoretical, simulated, and experimental cases, separately. a, b denote the two cases to be compared. The greater F value indicates that the experimental result is closer to the simulation result, and F will be equal to 1 if $|\psi_a\rangle = |\psi_b\rangle$. Here $F_{\text{sim,theo}}$ of $|\Psi_5\rangle, |\Psi_8\rangle, |\Psi_9\rangle, |\Psi_{10}\rangle$ are calculated as 0.998, 0.987, 0.992, and 0.986, respectively; $F_{\text{exp,theo}}$ of them are measured as 0.832, 0.855, 0.875, and 0.902, separately. The simulation is in precise agreement with theoretical values, while the experimental and theoretical values are basically consistent.

As for the selective-blocking cases, the experimental results are shown in Fig. 4(a) with the states selection of $|\Psi_k\rangle$, where the spatial filter placed at the separation plane is presented as Sp_2 . In other words, the bottom half of the separation plane is blocked.

The experimental intensities are generally as expected: the petaloid input patterns are converted into doughnut patterns after the blocking. The calculated $F_{\text{sim/theo}}$ of $|\Psi_5\rangle, |\Psi_8\rangle, |\Psi_9\rangle, |\Psi_{10}\rangle$ are 0.998, 0.988, 0.991, and 0.988; their measured $F_{\text{exp/theo}}$ are 0.804, 0.876, 0.838, and 0.880. These experimental performances also meet expectations. Figure 4(b) gives the experimentally measured TAM spectrum of the input and output beam, illustrating that the TAM processor has the ability to choose any TAM states on demand (see Fig. S18 in the [Supplementary Material](#) for simulated results).

Theoretically, the incident beam $|\Psi_l\rangle$ converts into a classical nonseparable state, denoted as $|\Psi'_l\rangle = |L\rangle| -l\rangle + |R\rangle|l\rangle$ in the selective-blocking cases using a spatial filter, represented as Sp_2 in Fig. 4. Such a process could be regarded macroscopically as a mode transformation from a twofold multiplexed OAM mode with horizontal linear polarization into a cylindrical vector mode with anisotropic polarization distributions. Therefore, an additional rotating polarizer is placed before the CCD camera for an anisotropic polarization measurement, whose experimental results are given in Fig. 5. For the input beam $|\Psi_6\rangle$, its intensity conforms to Marius' law. Meanwhile, the theoretical rotation angle of the output pattern should be θ/l , where θ is the rotation

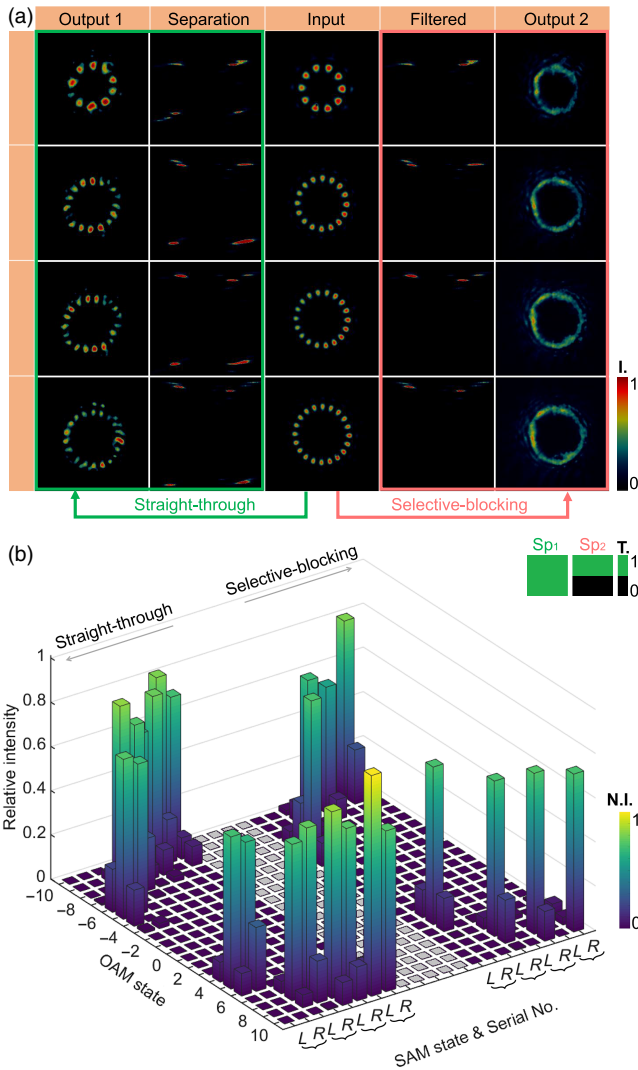


Fig. 4 Performance of the manipulator in straight-through and selective-blocking cases when multi-TAM states are incident. (a) Experimental results for incident beams $|\Psi_5\rangle$, $|\Psi_8\rangle$, $|\Psi_9\rangle$, $|\Psi_{10}\rangle$, where output 1 is the output intensity distributions in straight-through cases, and output 2 is the output intensities distributions in selective-blocking cases. The second column is the intensity distribution at separated plane without filtering, and the fourth column is the intensity distribution at that plane after filtering. (b) TAM spectra of the output beams in the above two cases. The OAM modes are represented by topological charge, and the SAM modes are represented as L and R . The TAM spectrum distribution diagram can be divided into two parts with the gray part as the boundary, representing the results of the straight-through cases and the selective-blocking cases, respectively. Sp_1 and Sp_2 are the filter masks for the two cases, separately.

angle of the polarizer.⁴⁵ Therefore, the rotation angle θ_1 of the output pattern should be 7.5 deg and 15 deg when the polarizer rotates 45 deg and 90 deg, separately, corresponding to typical anisotropic polarization distribution. The measured results are $\theta_1 = 7.87$ deg, $\theta_2 = 14.83$ deg and conform with the theoretical value.

The multi-TAM states experiment demonstrates the capacity of the system to simultaneously manipulate SAM and OAM

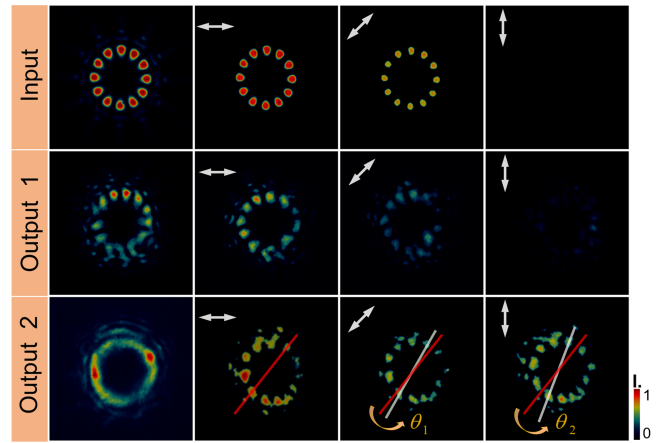


Fig. 5 Polarization distributions of experimental input and output beams. The input row shows the intensities of input beam. Output 1 is the intensity of the output beam at pass-through cases. Output 2 is the intensity of the output beam at selective-blocking cases. The arrow represents the direction of the polarizer, and the first column is the result with no polarizer.

modes, while the ability of OAM filtering with adjacent modes is the basic requirement for satisfying diversified manipulation. A horizontally polarized incident beam carrying adjacent OAM modes, denoted as $|\Psi_\Omega\rangle = (|L\rangle + |R\rangle)(|+9\rangle + |+10\rangle)$, is employed. Figure 6(a) displays the intensity distribution of the input, separation (filter), and the output plane, for the straight-through and selective-blocking cases. The output pattern is similar with the inputs at the straight-through cases, and the distribution of the separated plane conforms to the analysis in Note 4 in the [Supplementary Material](#). For the selective-blocking cases, adopting a spatial filter shown as Sp_2 in Fig. 6 for concurrently filtering the OAM mode $|+10\rangle$ and the two SAM modes, the output pattern converts from a notched ring into a complete ring.

Figure 6(b) gives the experimentally measured TAM spectrum of the output beam for the two cases. For straight-through cases, the calculated $F_{\text{sim}/\text{theo}}$ is 0.865 and $F_{\text{exp}/\text{theo}}$ is measured as 0.852, while $F_{\text{sim}/\text{theo}}$ is calculated as 0.823 and the measured $F_{\text{exp}/\text{theo}}$ is 0.772 for selective-blocking cases. The indicators and the patterns at the separation plane reveal that the filtered pattern and the filtered TAM spectrum are nonideal, which could be associated with the reduction in the focal length of L_2 by half and the incident OAM beam without amplitude modulation (the Laguerre–Gaussian mode incident will get the ideal result). Therefore, the difference between the simulation and theory should be taken into account. The calculated $F_{\text{exp}/\text{sim}}$ is 0.898 for straight-through cases, and it is 0.827 for selective-blocking cases, illustrating that the experimental performance and the simulation are analogous, but both of them have gaps from the theory. Unlike the previous set of experiments, there will be a nonnegligible deviation when the incident beam without Laguerre–Gaussian amplitude modulation in the case of the carrying adjacent OAM modes.

4 Discussion and Conclusions

In summary, we have proposed a scheme for manipulating TAM states of photons. It is carried out by symmetrically cascading two analogous units. The TAM separator achieving a separation

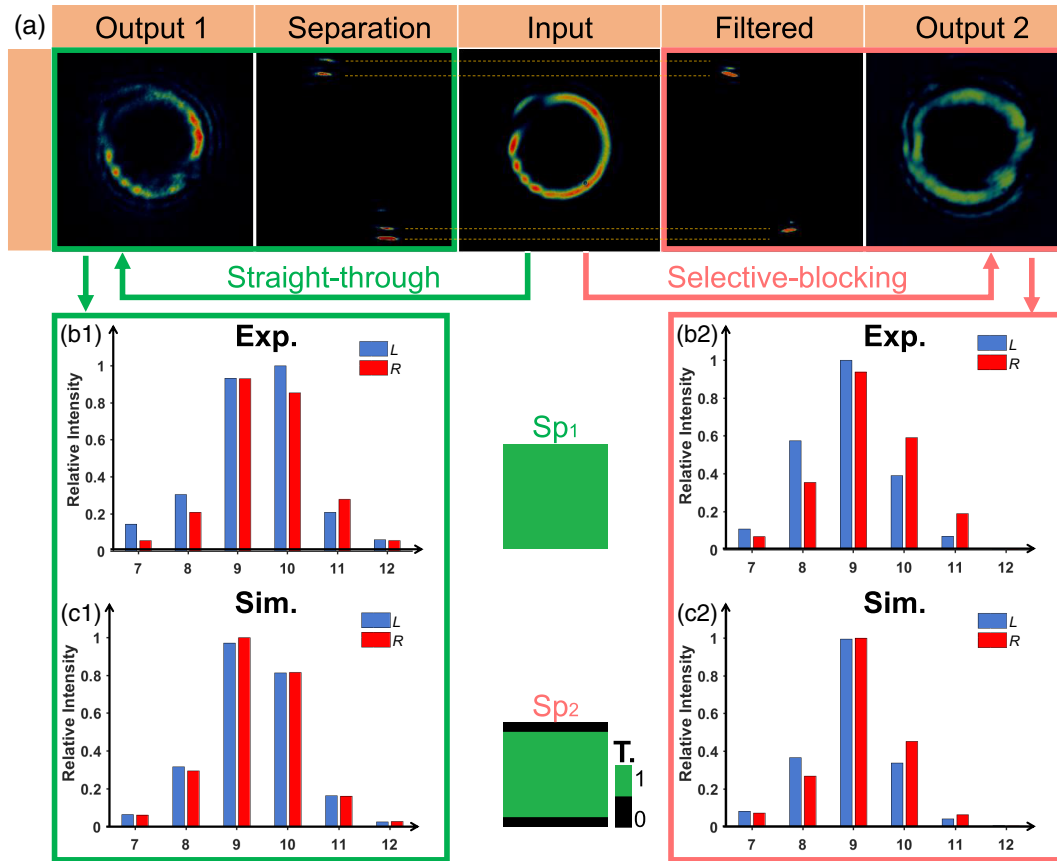


Fig. 6 Performance of the manipulator in straight-through and selective-blocking cases when adjacent OAM states are incident. (a) Experimental results for incident beams $|\Psi_\Omega\rangle$, where output 1 is the output intensity distribution in straight-through cases, and output 2 is the output intensity distribution in selective-blocking cases. The second column is the intensity distribution at the separated plane without filtering, and the fourth column is the intensity distribution at that plane after filtering. The dashed lines between the second and the fourth columns are references for the location of the separated modes. (b1), (b2) The experimental TAM spectrum of output beams in the straight-through cases and selective-blocking cases, respectively, where left and right circular polarizations are denoted as blue and red color bars; the ℓ axis means the eigenvalue of the OAM mode. Sp_1 and Sp_2 are the filter mask for the two cases, separately. (c1), (c2) Corresponding simulated results.

of arbitrary input TAM states could be understood as a transformation from the spatial domain into the position-TAM domain, where the incident beams are distributed as a set of nonseparable single TAM states in the position-TAM domain (the separation plane); the TAM reverser performs an opposite transformation, converting the beam back to the spatial domain. Our concept is supported by simulated and observed data.

The number of supported TAM states is determined by the following factors. Limited by the fabricated technique of GPOEs, the phase modulation exhibits deviation, which is shown in Note 7 in the [Supplementary Material](#). Since the diameter of OAM beams increases with the absolute value of topological charge l , the area illuminated on the fabricated elements is limited for the incidence of low-order OAM modes, resulting in more insufficient phase modulation than that of the high-order modes. As for the high-order OAM mode, it is restricted by the Fresnel number of the designed elements.³⁵ In other words, the inadequate phase modulation of low-order OAM modes and OAM cross talk of high-order modes limit the range of

supporting states. The number of supported TAM states can be improved by increasing the resolution of OAM separation, such as increasing the radius of the incident beam and reducing the distance between the unwrapper and corrector. As for other nonideal results in experiments, the input beam should change into the Laguerre–Gaussian mode; these four GPOEs need to be aligned more precisely or be integrated.

This work provides an idea for simultaneously tailoring OAM and SAM modes, extending the way for many state-of-the-art explorations. To date, a series of computing schemes have been proposed in the OAM domain, such as OAM multiplier,⁴⁶ OAM divider,⁴⁷ and unitary operation.¹² These operations can also be expanded to the TAM domain, which will enhance the versatility of optical computing. In conclusion, this work provides a scheme to manipulate TAM states on demand and attains the transformation from separable states to nonseparable states. The experiment demonstrates four-modes input, with two modes filtered, fitting well with the simulation. The TAM processor could be used in optical interconnects, optical computing,

and quantum technique. Facing the potentially complex manipulation requirements, the spatial filter implemented in the separation plane should be programmable. Using a polarization-insensitive and programmable device like digital micromirror devices as the filter and folding the optical path may be a future effort.

5 Appendices

5.1 Numerical Simulation

The diffraction fields when TAM beams passing through the TAM processor were calculated through the diffraction angular spectrum theory.⁴⁸ The modulation phase of unwrapper and corrector was defined on a mesh of 2000 pixels \times 2000 pixels. And the theoretical TAM spectrum analysis of the output beams was implemented on the basis of spiral harmonic decomposition.²⁶

5.2 Elements Fabrication

As the non-contact photoalignment method is implemented to produce the GPOEs, it can avoid mechanical damage, dust smirch, and static electricity.⁴⁹ It has the advantages of high quality and high resolution when processing multidomain orientation LCs. The substrates of LCs are spin-coated with a layer of dye molecules, which have the characteristics of photoisomerization and dichroic absorption. When irradiated by a polarized ultraviolet beam, the molecules tend to reorient their absorption oscillators perpendicular to the polarization. They will subsequently determine the orientation of the LCs. However, the reorientation of each LC molecule is also influenced by adjacent molecules, resulting in difficulty in achieving a perpendicular orientation between adjacent molecules. The orientation deviation is ~ 2 deg, causing the imperfect phase modulation of GPOEs.

To achieve effective resolution of TAM separation, the introduced wave-copying number is set to 3. Then the unwrapper and corrector are fabricated under the parameters of $\lambda = 1617$ nm, $d = 2$ mm, $b = 4$ mm, $c = [1.32, 1, 1.32]$, $N = 1$, $\zeta = [-\pi/2, 0, \pi/2]$, $\delta_1 = 0.5$ mm, $f_1 = 50$ mm, $\delta_2 = 2.5$ mm, $f_2 = 400$ mm, $\varphi = [0, 3\pi/2, 0]$, and the resolution is 2000×2000 . The fabricated elements consist of a large number of LC cells with the pixel pitch $5 \mu\text{m}$, whose main axes are arranged as our design. To introduce the geometric phase, each cell must act as a sub-half-wave plate, and $2\pi(n_{\text{eff}} - n_o)d/\lambda = \pi$ must be satisfied, where n_{eff} denotes the effective extraordinary refractive index determined by a molecule's tilting, n_o denotes the ordinary refractive index, d is the LC cell gap, and λ is the wavelength.

5.3 Experimental Characterization

As for the TAM states preparation, a self-developed distributed feedback laser diode with the wavelength 1617 nm was adopted as the source to produce a laser beam. Then the beam was shaped by a single-mode fiber and was coupled into free space from a collimator with a diameter of 3 mm. The TAM states were generated by encoding specially designed holograms on a spatial light modulator (Holoeye, PLUTO-TELCO-013-C), associated with a series of polarization elements.

The experimental setup of the TAM processor essentially was consistent with the theoretical analysis, while the focal

lengths of the second and third lenses L_2 and L_3 were changed to 200 mm, due to the size limitations of the optical platform. The four GPOEs were mounted on the six-axis locking kinematic mounts (AMM6-1A, Lbtek).

Infrared CCD cameras (Cobra2000-CL1280-130vt-00, LUSTER) were employed to capture patterns of input beams, separated beams, and output beams. Finally, the projection measurement²⁶ was implemented to analyze the TAM spectra of output beams.

Code, Data, and Materials Availability

The simulated and experimental data that support this work are available from the corresponding author upon reasonable request.

Acknowledgments

We would like to acknowledge Mr. Lei Huang and Mr. Yanlai Lv for helpful discussions when doing this work. This work was supported by the National Key Research and Development Program of China (Grant No. 2022YFB3607700), the National Natural Science Foundation of China (Grant Nos. 11834001 and 61905012), the National Defense Basic Scientific Research Program of China (Grant No. JCKY2020602C007), the Beijing Natural Science Foundation (Grant No. 1232031), the Special Fund for Basic Scientific Research of Central Universities of China (Grant No. 2022CX11006), and the National Postdoctoral Program for Innovative Talents (Grant No. BX20190036).

References

1. R. A. Beth, "Mechanical detection and measurement of the angular momentum of light," *Phys. Rev.* **50**, 115–125 (1936).
2. L. Allen et al., "Orbital angular momentum of light and the transformation of Laguerre–Gaussian laser modes," *Phys. Rev. A* **45**, 8185–8189 (1992).
3. S. Fu and C. Gao, "Basic characteristics of vortex beams," in *Optical Vortex Beams: Advances in Optics and Optoelectronics*, S. Fu and C. Gao, Eds., pp. 41–62, Springer, Singapore, (2023).
4. J. Wang et al., "Terabit free-space data transmission employing orbital angular momentum multiplexing," *Nat. Photonics* **6**, 488–496 (2012).
5. N. Bozinovic et al., "Terabit-scale orbital angular momentum mode division multiplexing in fibers," *Science* **340**, 1545–1548 (2013).
6. S. Fu et al., "Demonstration of free-space one-to-many multicasting link from orbital angular momentum encoding," *Opt. Lett.* **44**, 4753–4756 (2019).
7. J. Wang et al., "Twisted optical communications using orbital angular momentum," *Sci. China Phys. Mech. Astron.* **62**, 34201 (2019).
8. Y. Yang et al., "Optical trapping with structured light: a review," *Adv. Photonics* **3**, 034001 (2021).
9. M. P. J. Lavery et al., "Detection of a spinning object using light's orbital angular momentum," *Science* **341**, 537–540 (2013).
10. S. Fu et al., "Non-diffractive Bessel–Gauss beams for the detection of rotating object free of obstructions," *Opt. Express* **25**, 20098–20108 (2017).
11. X. Fang, H. Ren, and M. Gu, "Orbital angular momentum holography for high-security encryption," *Nat. Photonics* **14**, 102–108 (2020).
12. S. Li et al., "Programmable unitary operations for orbital angular momentum encoded states," *Natl. Sci. Open* **1**, 20220019 (2022).
13. Y. Huang et al., "Versatile total angular momentum generation using cascaded J-plates," *Opt. Express* **27**, 7469–7484 (2019).

14. S. Liu et al., “Highly efficient generation of arbitrary vector beams with tunable polarization, phase, and amplitude,” *Photonics Res.* **6**, 228–233 (2018).
15. X. Yi et al., “Hybrid-order Poincaré sphere,” *Phys. Rev. A* **91**, 023801 (2015).
16. X. Wang et al., “Femtosecond laser-based processing methods and their applications in optical device manufacturing: a review,” *Opt. Laser Technol.* **135**, 106687 (2021).
17. L. Fang et al., “Vectorial Doppler metrology,” *Nat. Commun.* **12**, 4186 (2021).
18. R. Fickler et al., “Quantum entanglement of high angular momenta,” *Science* **338**, 640–643 (2012).
19. X. Wang et al., “18-qubit entanglement with six photons’ three degrees of freedom,” *Phys. Rev. Lett.* **120**, 260502 (2018).
20. S. Fu et al., “Diagnostics of the topological charge of optical vortex by a phase-diffractive element,” *Chin. Opt. Lett.* **14**, 080501 (2016).
21. C. Wan, J. Chen, and Q. Zhan, “Compact and high-resolution optical orbital angular momentum sorter,” *APL Photonics* **2**, 031302 (2017).
22. G. Ruffato et al., “A compact diffractive sorter for high-resolution demultiplexing of orbital angular momentum beams,” *Sci. Rep.* **8**, 10248 (2018).
23. J. Yang et al., “Two-dimension and high-resolution demultiplexing of coaxial multiple orbital angular momentum beams,” *Opt. Express* **27**, 4338–4345 (2019).
24. J. Cheng, C. Wan, and Q. Zhan, “High-resolution optical orbital angular momentum sorter based on Archimedean spiral mapping,” *Opt. Express* **30**, 16330–16339 (2022).
25. Y. Lv et al., “Sorting orbital angular momentum of photons through a multi-ring azimuthal-quadratic phase,” *Opt. Lett.* **47**, 5032–5035 (2022).
26. S. Fu et al., “Universal orbital angular momentum spectrum analyzer for beams,” *Photonix* **1**, 19 (2020).
27. J. Wang et al., “Adjusted EfficientNet for the diagnostic of orbital angular momentum spectrum,” *Opt. Lett.* **47**, 1419–1422 (2022).
28. Q. Jia et al., “Simultaneously sorting vector vortex beams of 120 modes,” arXiv.2212.08825 (2022).
29. J. Leach et al., “Measuring the orbital angular momentum of a single photon,” *Phys. Rev. Lett.* **88**, 257901 (2002).
30. C. Gao et al., “Sorting and detecting orbital angular momentum states by using a Dove prism embedded Mach–Zehnder interferometer and amplitude gratings,” *Opt. Commun.* **284**, 48–51 (2011).
31. W. Zhang et al., “Mimicking Faraday rotation to sort the orbital angular momentum of light,” *Phys. Rev. Lett.* **112**, 153601 (2014).
32. G. C. G. Berkhout et al., “Efficient sorting of orbital angular momentum states of light,” *Phys. Rev. Lett.* **105**, 153601 (2010).
33. M. Mirhosseini et al., “Efficient separation of the orbital angular momentum eigenstates of light,” *Nat. Commun.* **4**, 2781 (2013).
34. M. P. J. Lavery et al., “Measurement of the light orbital angular momentum spectrum using an optical geometric transformation,” *J. Opt.* **13**, 064006 (2011).
35. M. P. J. Lavery et al., “Efficient measurement of an optical orbital-angular-momentum spectrum comprising more than 50 states,” *New J. Phys.* **15**, 013024 (2013).
36. Y. Wen et al., “Spiral transformation for high-resolution and efficient sorting of optical vortex modes,” *Phys. Rev. Lett.* **120**, 193904 (2018).
37. H. Huang et al., “Tunable orbital angular momentum mode filter based on optical geometric transformation,” *Opt. Lett.* **39**, 1689–1692 (2014).
38. G. F. Walsh, “Pancharatnam–Berry optical element sorter of full angular momentum eigenstate,” *Opt. Express* **24**, 6689–6704 (2016).
39. H. Larocque et al., “Generalized optical angular momentum sorter and its application to high-dimensional quantum cryptography,” *Opt. Express* **25**, 19832–19843 (2017).
40. B. Wang et al., “Sorting full angular momentum states with Pancharatnam–Berry metasurfaces based on spiral transformation,” *Opt. Express* **28**, 16342–16351 (2020).
41. Y. Liu et al., “Photonic spin Hall effect in metasurfaces: a brief review,” *Nanophotonics* **6**, 51–70 (2017).
42. H. Wang et al., “Intelligent optoelectronic processor for orbital angular momentum spectrum measurement,” *Photonix* **4**, 9 (2023).
43. S. Zheng et al., “Experimental realization to efficiently sort vector beams by polarization topological charge via Pancharatnam–Berry phase modulation,” *Photonics Res.* **6**, 385–389 (2018).
44. W. J. Hossack, A. M. Darling, and A. Dahdouh, “Coordinate transformations with multiple computer-generated optical elements,” *J. Mod. Opt.* **34**, 1235–1250 (1987).
45. S. Fu et al., “Generating polarization vortices by using helical beams and a Twyman Green interferometer,” *Opt. Lett.* **40**, 1775–1778 (2015).
46. G. Ruffato, M. Massari, and F. Romanato, “Multiplication and division of the orbital angular momentum of light with diffractive transformation optics,” *Light Sci. Appl.* **8**, 113 (2019).
47. H. Zhou et al., “Orbital angular momentum divider of light,” *IEEE Photonics J.* **9**, 6500208 (2017).
48. J. Li, Z. Peng, and Y. Fu, “Diffraction transfer function and its calculation of classic diffraction formula,” *Opt. Commun.* **280**, 243–248 (2007).
49. P. Chen et al., “Liquid-crystal-mediated geometric phase: from transmissive to broadband reflective planar optics,” *Adv. Mater.* **32**, 1903665 (2019).

Lang Li is a PhD student at the Beijing Institute of Technology. He received his BS degree in optoelectronic information science and engineering from the Beijing Institute of Technology, Beijing, China, in 2020. He is currently working toward his PhD following Prof. Shiyao Fu in optical engineering at the School of Optics and Photonics, Beijing Institute of Technology, Beijing, China. His research interest concerns laser field tailoring, focusing on the related research of photon orbital angular momentum.

Chunqing Gao has been a professor at the School of Optics and Photonics, Beijing Institute of Technology, China, since 2001. He received his BS and MS degrees in optics from the Beijing Institute of Technology and his PhD in physics from the Technical University, Berlin, Germany. The current research in his group mainly focuses on innovative laser systems, laser beam manipulation, and related applications. He has published four books and more than 260 scientific papers in journals and conferences. He has 30 authorized patents in the fields of optics and lasers.

Shiyao Fu is currently a professor at the Beijing Institute of Technology. He received his PhD in electronic science and technology from the Beijing Institute of Technology in 2019. His current research interests cover complex structured field manipulation, innovative solid-state lasers, and their applications in critical engineering. He has published two books and more than 50 peer-reviewed papers. He has 20 authorized patents. He was selected for the national postdoctoral program for innovative talents. He is the recipient of the second prize of the Beijing Natural Science Award. He won the Wang Da-Heng Optics Prize, and his doctoral dissertation was recognized by the Chinese Institute of Electronics. He is a senior member of the Chinese Optical Society.

Biographies of the other authors are not available.